Role of microstructure reactivity and surface diffusion in explaining flash (ultra-rapid) sintering kinetics

Charles Manière, Christelle Harnois, Sylvain Marinel

Role of microstructure reactivity and surface diffusion in explaining flash (ultra-rapid) sintering kinetics

Charles Manière[1]*, Christelle Harnois[1], Sylvain Marinel[1]

1. Normandie Univ, ENSICAEN, UNICAEN, CNRS, CRISMAT, 14000, Caen, France

Keywords

Flash sintering; Coarsening; Surface diffusion; Mesoscale simulation; Spark Plasma Sintering

Abstract

The competition between sintering and coarsening is cited by numerous authors as one of the potential factors for explaining the ultra-rapid sintering kinetics of flash sintering. In particular, surface diffusion is a mechanism decreasing the driving force of sintering by changing the initial highly reactive microstructures (particle contact) into poorly reactive porous skeleton structures (spherical porosity). We show by finite element simulations that flash SPS experiments high specimen temperatures close to 2000°C. These high temperatures are not sufficient to explain the ultra-rapid sintering kinetics if typical spherical pore theoretical moduli are employed. On the contrary, reactive experimentally determined moduli succeed in explaining the ultra-rapid sintering kinetics. Mesoscale simulations evidenced that the origin of such reactive experimental moduli is a porous skeleton geometry with a significant delay in surface diffusion and particle rearrangement. This highlights the important role of the surface diffusion negation (favoring higher stress intensification factor) in flash sintering.

Graphical abstract

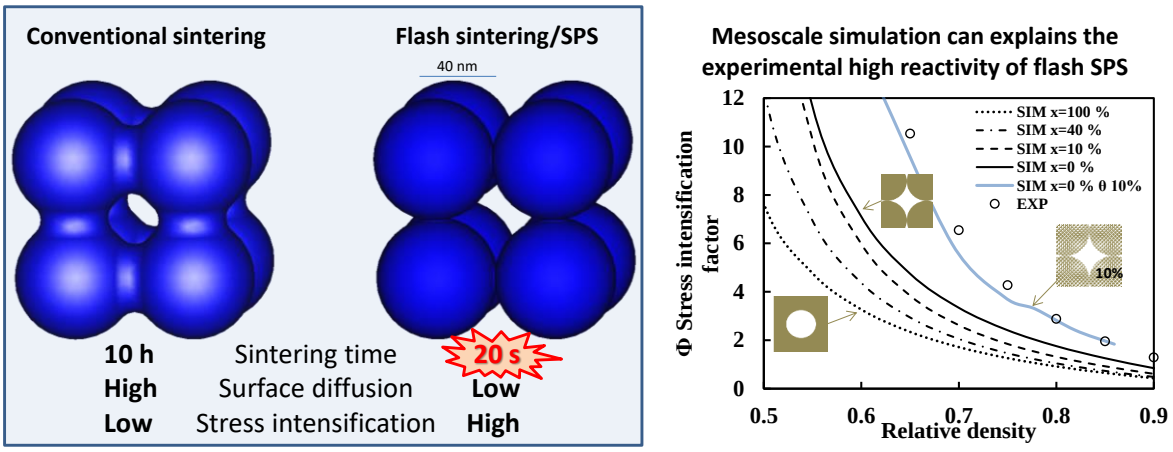

* Corresponding author: **CM**: Laboratoire de cristallographie et sciences des matériaux (CRISMAT), 6 Bvd du maréchal Juin 14050 CAEN CEDEX 4, France
Ph.: +33.2.31.45.13.69 ; *E-mail address*: charles.maniere@ensicaen.fr

Highlights

- ❖ Short sintering time of flash sintering implicates less surface diffusion
- ❖ Surface diffusion decrease makes higher stress intensification and sintering reactivity
- ❖ Demonstration of microstructure reactivity based on mesoscale simulation

Nomenclature

θ Porosity

$\dot{\theta}$ Porosity elimination rate (s^{-1})

ρ Relative density

$\underline{\sigma}$ Stress tensor ($N.m^{-2}$)

$\underline{s}$ Deviatoric stress tensor ($N.m^{-2}$)

σ_{eq} Equivalent stress ($N.m^{-2}$)

$\underline{\dot{\varepsilon}}$ Strain rate tensor (s^{-1})

$\dot{\varepsilon}_{eq}$ Equivalent strain rate (s^{-1})

n Creep law stress exponent

m Creep law grain size exponent

A Creep law deformability term ($s^{-1}Pa^{-n}$)

A_0 Deformability pre-exponential factor ($Ks^{-1}Pa^{-n}$)

Q Deformability activation energy ($J.mol^{-1}$)

R Gas constant 8.314 ($J.mol^{-1}.K^{-1}$)

T Temperature (K)

φ Shear modulus

ψ Bulk modulus

Pl Sintering stress (Pa)

$\mathbb{i}$ Identity tensor

α Surface energy ($J.m^{-2}$)

r Particles radius (m)

P Hydrostatic stress ($N.m^{-2}$)

τ Shear stress invariant ($N.m^{-2}$)

$\dot{\varepsilon}_r$ Radial strain rate tensor component (s^{-1})

$\dot{\varepsilon}_z$ Axial strain rate tensor component (s^{-1})

σ_r Radial stress tensor component ($N.m^{-2}$)

σ_z Axial stress tensor component ($N.m^{-2}$)

s_r Radial deviatoric stress tensor component ($N.m^{-2}$)
s_z Axial deviatoric stress tensor component ($N.m^{-2}$)
θ_c Critical porosity
μ Bulk modulus exponent
a, b, c Fitting constants
t Time (s)
H A constant
D Diffusion coefficient ($m^2.S^{-1}$)
k Boltzmann Constant ($1.380\ 649 \times 10^{-23}\ J.K^{-1}$)
ϕ Stress intensification factor
SPS Spark Plasma Sintering

1. Introduction

Flash sintering is a very interesting process involving sintering times of few seconds and a significant energy saving compared to conventional processes requiring hours of processing[1–5]. Since the discovery of the flash phenomenon in 2010[6,7], numerous possible mechanisms have been proposed for explaining such ultra-rapid sintering mechanism. Among them, we can cite the current/field effect[5,8,9] such as the ponderomotive forces[10–12], electroplasticity[9,13,14], electromigration[15]. For the thermal effects, we can also cite the thermodiffusion[16], grain boundary heating[5,6] and reduced coarsening kinetics[17–19]. The latter is studied in the present article and reduces the densification kinetics by extending the diffusional distances and by reducing the capillarity forces at the necks. This aspect is often studied by coupling the densification model with grain growth[20–25]. Such model allows to predict the final stage reduction of the sintering kinetics and the sintering trajectory. The last aspect is very interesting to conduct optimizations of the thermal cycle[26].

Among the coarsening mechanisms, the surface diffusion mechanism also competes with densification having material sources at the center of the grain boundary. Surface diffusion redistributes the material at the pore surface diminishing the pore surface energy to gradually form a spherical pore. This spheroidization process of the porosity shape is accompanied by a

significant decrease of the sintering driving force[17]. In the case of SPS which is studied in this paper, this reduction involves less capillarity forces (higher porosity neck radii) and a less effective stress in the active zone of sintering (the grain boundary). The latter phenomenon is represented by the stress intensification factor Φ defined in the typical analytical hot pressing model below [27].

$$-\dot{\varepsilon}_z = \frac{1}{\rho}\frac{d\rho}{dt} = \frac{HD(T)\phi(\rho)^n\sigma_z^n}{G^m kT} \quad (1)$$

In this equation (1), $n = 1$, $m = 2$ correspond to lattice diffusion, $n = 1$, $m = 3$ to grain boundary diffusion, and $n = 1$ or 2, $m = 1$ to grain boundary sliding and $n > 3$, $m = 0$ to dislocation based creep.

The stress intensification factor (see figure 1) is a function of the porosity that is defined as the ratio between the area of a small element unit cell (A_1) and the grain boundary area (A_{gb}), giving $\Phi = A_1/A_{gb}$. This parameter is strongly impacted by the porosity shape. In conventional sintering, the long sintering time allows advanced pore surface shape redistribution (large curvature radius, microstructure on the right in figure 1). For flash sintering, the few seconds of sintering time which significantly delay the surface diffusion may result in the preservation of the initial reactive porous skeleton characterized by higher stress intensification factor (microstructure on the left in figure 1) [17]. This factor is generally assumed as a unique function of the porosity and approximated theoretically[27–31]. However, considering the surface diffusion in conventional *vs* flash sintering, it appears clearly that at the same porosity, flash sintering with reduced surface diffusion may result in higher values of Φ (see A_{GB} evolution in figure 1 at θ=15%).

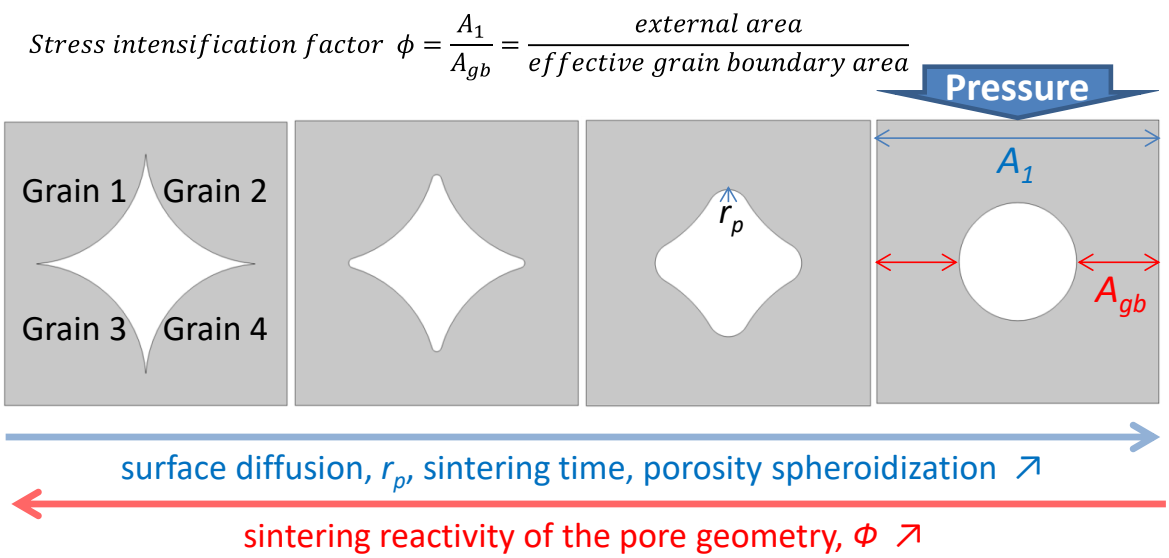

Figure 1 2D scheme of the porosity spheroidization of a 4-grain model at constant porosity (15%) under the action of surface diffusion; correlation with the stress intensification factor, this shape evolution strategy will be applied in 3D structures of a half particle.

The flash sintering densification kinetics are generally not explained by the conventional model[5]. The question is then to know which mechanism cited earlier is responsible for this fast sintering response. In this article we explore the impact of the surface diffusion on the porosity shape and then on the stress intensification factor. It is difficult to determine the porosity function of the stress intensification factor experimentally, without risk of disturbance with other microstructure development terms like grain growth. However, we recently find a method based on instrumented sinter-forging tests able to determine separately these parameters for zirconia[32]. This study investigates the sinter-forging in a stable grain size zone below 90% of densification[33]. Using the SPS sinter-forging moduli, we were able to reproduce the flash SPS curve [34]. This suggests the identified moduli were reactive enough to explain the sintering kinetics as fast as flash SPS. Because latter identification was conducted in isothermal/insulated conditions after a fast heating (100 K/min); we suspect that short heating and the fast sintering time of SPS (~15min) enable to identify parameters with less impact of surface diffusion and preservation of the initial microstructure reactivity. In order to test this impact indirectly *via* stress intensification factor, we will try to explain the reactivity of the experimental stress intensification factor with mesoscale simulations that take

different geometrical hypotheses of porosity and different levels of porous shape reactivity (from sharp edges to spherical pores).

2. Theory and calculations

The continuum theory of sintering is detailed in[35] and the details of the analytical equations of SPS are detailed in [32]. In this section, we will develop the formulation of the equivalent mesoscale simulation equations. These equations will be used to identify the equivalent shear and bulk sintering behavior of the zirconia specimen for different porous skeleton hypotheses.

2.1. Analytic formulation of SPS

In this study the Skorohod-Olevsky model of sintering [35] is employed. This continuum model can be implemented in a finite element code. In order to determine the sintering behavior before conducting simulations, analytical equations can be defined for each specific sintering case like free-sintering, sinter-forging, isostatic pressing or hot pressing. The analytics equation of hot pressing (2) is very useful to describe the sintering under SPS conditions.

$$\dot{\varepsilon}_z = A(T,G)\left(\psi + \frac{2}{3}\varphi\right)^{\frac{-n-1}{2}}(1-\theta)^{\frac{1-n}{2}}(\sigma_z - P_l)^n \qquad (2)$$

This formula can be compared with the solid-state model (1) of hot pressing that neglects the capillarity forces ($P_l = 0$).

The link between the stress intensification factor ϕ that depends on the pore geometry and the shear (φ) and bulk (ψ) moduli appears clearly.

$$\phi = \left(\left(\psi + \frac{2}{3}\varphi\right)^{\frac{-n-1}{2}}(1-\theta)^{\frac{1-n}{2}}\right)^{\frac{1}{n}} \text{ and } A(T,G) = \frac{HD(T)}{G^m kT} \qquad (3)$$

It is clear in equations (1), (2) and (3) that a higher stress intensification factor and consequently lower moduli (φ, ψ) result in higher densification kinetics $\frac{1}{\rho}\frac{d\rho}{dt}$.

In this article we will compare the experimental moduli with mesoscale simulated moduli to determine if SPS and flash SPS ultra-rapid densification kinetics can be explained by reactive porous geometry resulting in a less effective surface diffusion. In the section below, the analytical equations employed to extract the moduli from the mesoscale simulation are described. A 2D-axisymmetric simulation of a die compaction configuration will be explored to determine an approximation of the 3D geometry with low computation times.

2.2. Mesoscale equivalent die pressing test identification equations

The following general formulas (4) are considered for the Skorokhod-Olevsky continuum model. Analytic die pressing equations (typical SPS configuration) will be considered starting from these general equations to identify the shear ad bulk moduli from the mesoscale simulations.

$$\underline{\dot{\varepsilon}} = A{\sigma_{eq}}^{n-1}\left(\frac{\underline{s}}{\varphi} + \frac{(P-P_l)}{3\psi}\underline{\underline{\mathbb{I}}}\right), and\ \sigma_{eq} = \frac{\sqrt{\frac{\tau^2}{\varphi}+\frac{(P-Pl)^2}{\psi}}}{\sqrt{1-\theta}} \quad (4)$$

The mesoscale model idealizes the SPS die pressing case by a Representative Elementary Volume (REV) where different porous skeleton geometries are tested. With the numerical information of the axial (Z) stress (σ_z) and strain rate ($\dot{\varepsilon}_z$) and the radial (R) stress (σ_r), it is possible to determine numerically the shear and bulk modulus.

Neglecting the capillarity stress P_l, the identification consists of a system of two equations using the following term ($Z(\theta)$) originating from the equation (2) in axial direction (Z).

$$\psi + \frac{2}{3}\varphi = \left(|\dot{\varepsilon}_z|^{-\frac{1}{n}}(1-\theta)^{\frac{1-n}{2n}}A^{\frac{1}{n}}|\sigma_z|\right)^{\frac{2n}{n+1}} = Z(\theta) \quad (5)$$

In radial direction (R), no displacement occurs and equation (4) becomes:

$$\dot{\varepsilon}_r = A{\sigma_{eq}}^{n-1}\left(\frac{s_r}{\varphi} + \frac{tr(\underline{\sigma})}{9\psi}\right) = 0 \quad (6).$$

With the radial deviatoric stress expression $s_r = \frac{\sigma_r - \sigma_z}{3}$, it is possible to determine the following ratio to the radial and axial stresses.

$$\frac{\sigma_r}{\sigma_z} = \frac{\psi - \frac{1}{3}\varphi}{\psi + \frac{2}{3}\varphi} \tag{7}$$

Then, rearranging (5) and (7), it is possible to obtain the following system of equations (8) allowing the shear and bulk modulus determination from the simulated data, in particular the calculated radial and axial stress ratio.

$$\begin{cases} \varphi = Z(\theta)\left(1 - \frac{\sigma_r}{\sigma_z}\right) \\ \psi = \frac{Z(\theta)}{3}\left(1 + 2\frac{\sigma_r}{\sigma_z}\right) \end{cases} \tag{8}$$

If P_l is not neglected, the new term $Z'(\theta)$ is expressed as:

$$\left(\psi + \frac{2}{3}\varphi\right) = \left(\dot{\varepsilon}_z{}^{-1} A(T,G)(1-\theta)^{\frac{1-n}{2}}(\sigma_z - P_l)^n\right)^{\frac{2}{n+1}} = Z'(\theta) \tag{9}.$$

The term P_l of the mesoscale model was determined by the resulting capillarity compressive stress on the cell and assuming flat grain boundary. The local surface stress (σ_{surf}) was imposed on the porosity curved surfaces by the following formula that takes the two principal surfaces radii of curvature (r_1 and r_2).

$$\sigma_{surf} = \alpha\left(\frac{1}{r_1} + \frac{1}{r_2}\right) \tag{10}$$

Using a similar method for the determination of equation (7), the new radial/axial stress ratio is,

$$\frac{\sigma_r}{\sigma_z} = \frac{\left(\psi - \frac{1}{3}\varphi\right) + \frac{\varphi Pl}{\sigma_z}}{\psi + \frac{2}{3}\varphi} \tag{11}.$$

Finally, the new identification system of equations considering the capillarity stress P_l is the following.

$$\begin{cases} \varphi = Z'(\theta)\frac{\left(\frac{\sigma_r}{\sigma_z} - 1\right)}{\left(\frac{Pl}{\sigma_z} - 1\right)} \\ \psi = Z'(\theta)\left(1 - \frac{2}{3}\left(\frac{\frac{\sigma_r}{\sigma_z} - 1}{\frac{Pl}{\sigma_z} - 1}\right)\right) \end{cases} \tag{12}$$

3. Method

In this work, the sintering response of moduli identified experimentally and by mesoscale simulation is investigated. In a first step, two insulated die SPS tests at 100 and 1000K/min (see figure 2) are studied to compare the potential of experimentally obtained moduli and theoretical ones to reproduce the SPS and flash SPS densification kinetics. To compare the sintering with previously identified moduli [32], the same zirconia powder was used (tosoh TZ-3Y-E). The expression of experimental moduli identified for the TZ-3Y-E powder is detailed below.

$$\varphi = \left(1 - \frac{\theta}{0.6}\right)^{3.4} \tag{13}$$

$$\psi = 0.07\,\frac{(1-\theta)^{5.8}}{\theta} \tag{14}$$

The simulated sintering response will be explored using these moduli and different theoretical moduli. An electro-thermal-mechanical-microstructural (ETMM) model[34] is employed to simulate the thermal gradients that significantly raise the effective specimen temperature. The two SPS tests (100 and 1000K/min) used a constant applied pressure of 50 MPa. These two tests data and their ETMM simulation conditions are reported in our previous article[34]. All the physical properties used in the simulation are reported in the appendix (table A), the electrical properties taken for zirconia used the *in situ* measurement data of ref[36] that were conducted in vacuum.

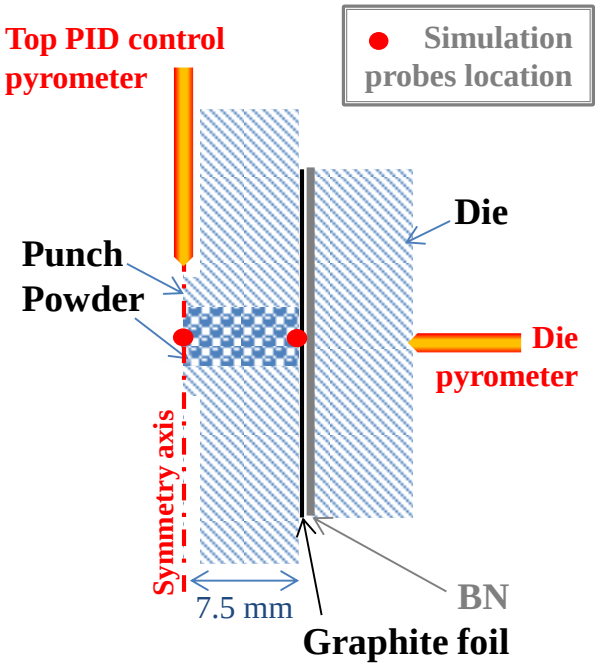

Figure 2 Configuration of the 15mm diameter SPS tests conducted at 100 K/min and 1000 K/min, the location of the two pyrometers and simulation temperature probes are indicated by the red arrow and points.

In a second step, mesoscale simulations are employed to identify simulated moduli corresponding to different pore skeleton hypotheses. The impact of surface diffusion is tested not by surface diffusion kinetics but by different particles contact geometries with different neck radii of curvature. The grain boundary dimension is tuned to explore different relative densities for the same neck radii of curvature. When the neck radii of curvature are similar to the particle radii, the porosity becomes nearly circular and the 3D revolution gives a torus shape similar to the cylindrical porosity geometry employed by Coble [37] in intermediate stage sintering. This torus shape corresponds to the case where surface diffusion dominates (low reactivity case close to spherical pore case); on the contrary, low neck radii correspond to the particle contact case with delayed surface diffusion and high stress intensification. The configuration is reported in figure 3. Two rigid materials with slip and no penetration conditions are used to press the particle and confine it radially (like in SPS). The radial force exerted on the vertical rigid material is measured to calculate the radial stress σ_r on the lateral surface during the densification. With the information of σ_r, σ_z, $\dot{\varepsilon}_z$ and the creep properties of

zirconia *A*, *n* [32], the shear and bulk moduli can be determined using (8) and also (12) if the sintering stress P_l is considered.

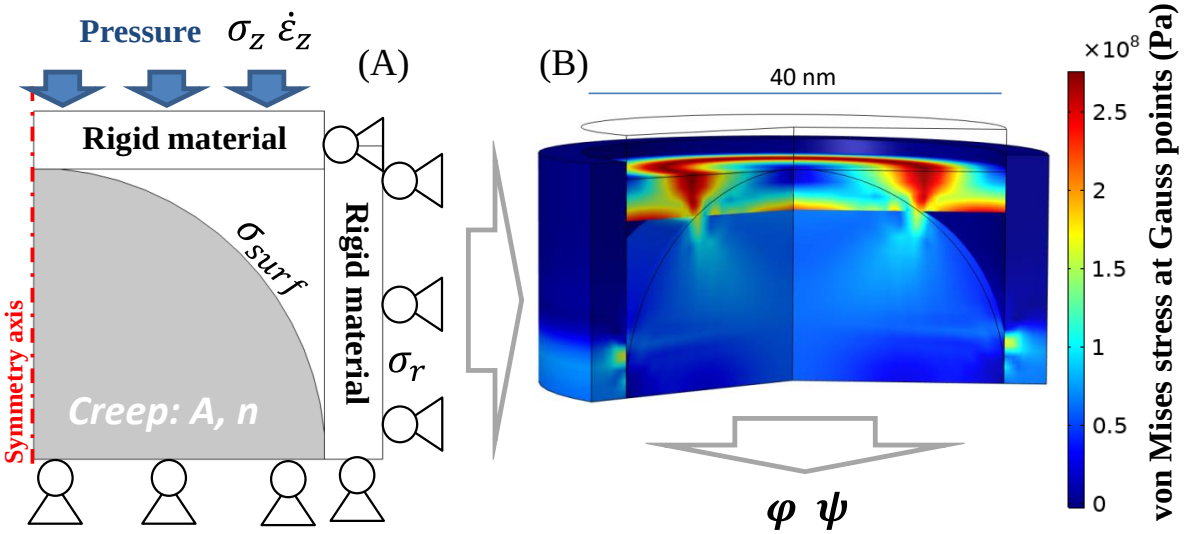

Figure 3 Geometry of the 3D microstructures approximation in the mesoscale simulation; 2D-axisymmetric simulations at mesoscale, configuration, boundary conditions (A) and simulation capture of the von Mises stress distribution of a pressed particle (B).

In the third step, the stress intensification factors will be compared to estimate the underlying reactivity of the porous skeletons.

4. Results and discussion

4.1. FEM simulation of SPS and flash SPS Joule heating

One of the pending questions in explaining the flash sintering ultra-rapid densification kinetics is to know if the temperature measurement does not underestimate the real specimen temperatures. It is well-known that SPS thermal gradients are present between the center and the edge of the device [38–42]. In SPS, the electric and thermal contact resistances present at all internal interfaces play a major role in the development of these gradients [43]. In a previous study [34,44,45], we have shown that the thermal contact resistance tends to generate an important thermal confinement of the heating of the specimen at high temperature. The thermal contact resistance tends then to magnify the temperature difference

between the specimen and the measurement location. The faster the heating is, the higher this temperature difference is [34]. In flash heating conditions, it is not excluded that effective specimen temperatures close to the melting point explain the fast densification kinetics. In order to test this hypothesis, we conduct a FEM simulation of the two SPS tests at 100 K/min and 1000 K/min. The results are reported in figure 4 for the heating.

In these experiments, the two pyrometers measure the temperature in the punch hole near the sample and at the die surface. Four virtual probes measure the temperature in the same location and in the specimen center and edge. It is interesting to see the concentrated current profile which results from the insulated die and the selective heating in the powder resulting from the thermal contact resistances. At 100 K/min, the temperature distribution shows a difference of about 200K between the temperature control of the punches and the maximum specimen temperature. As expected, at 1000 K/min, this temperature difference is greatly increased and becomes 700K with a maximum temperature in the specimen center of 2100°C. In the section, we will compare the sintering response of these temperatures for different sintering moduli hypotheses.

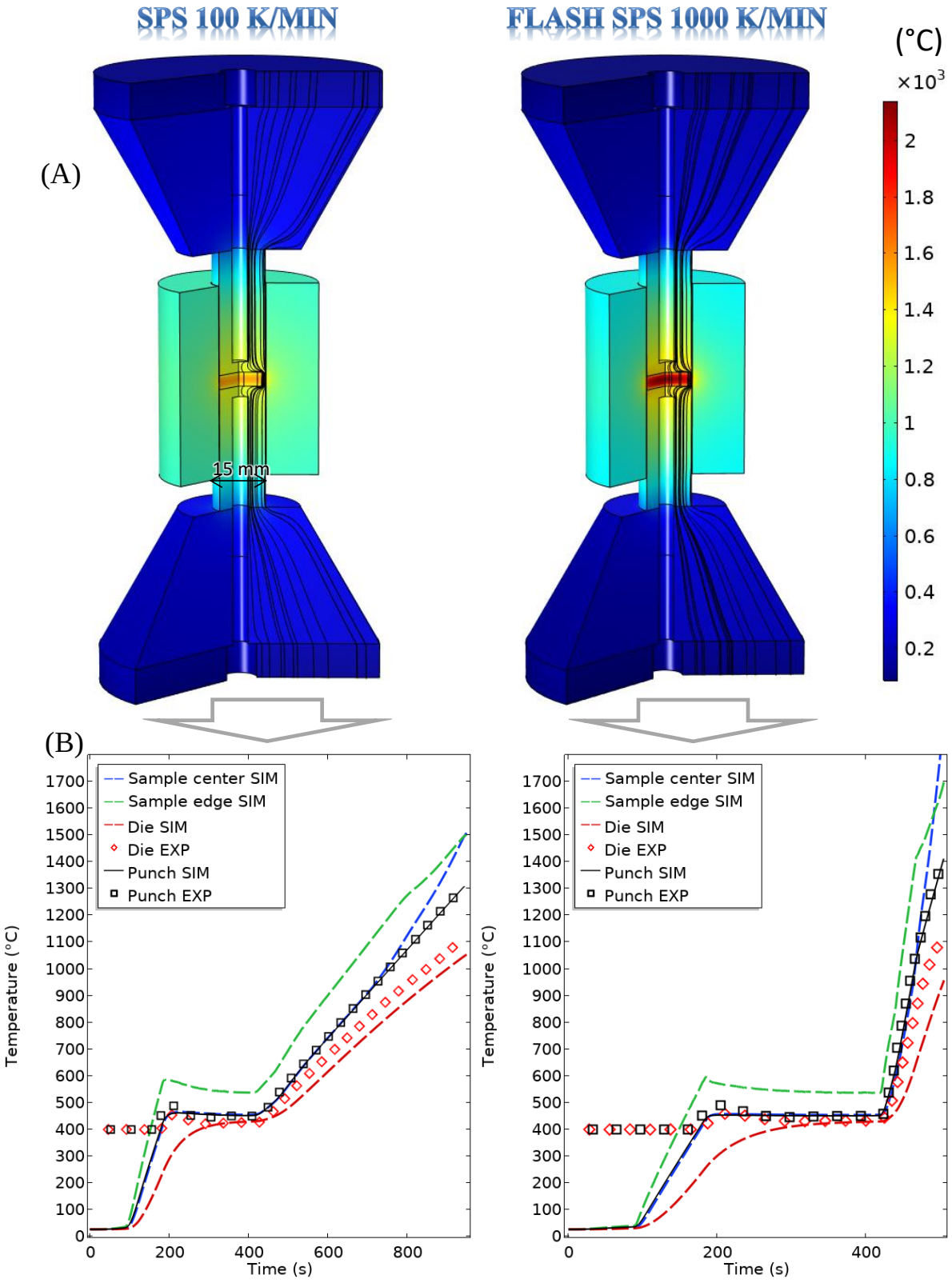

Figure 4 FEM Joule heating simulation of the SPS 100 K/min and 1000 K/min flash SPS, simulated thermal field at the end of heating (A), simulated temperature curves at different locations of the pressing device (B), two virtual probes are added to know the specimen temperature at the center and the edge.

4.2. FEM simulation of SPS and flash SPS densification

The relative density and sintering shrinkage of the two experiments simulated previously are reported in figure 5. These calculations employ the creep/moduli parameters and grain growth law of TZ-3Y-E zirconia identified by sinter-forging tests in [34] (see experimental the grain growth equation below).

$$\dot{G} = \frac{0.04[m^{1+p}.ss^{-1}]\exp\left(\frac{-575[kJ/mol]}{RT}\right)}{G^{1.63}} \quad (15)$$

In 1981, Harmer and Brook [46] showed fast firing can favorably enhance the densification over the coarsening kinetics at high temperatures if the grain growth activation energy is smaller than the sintering activation energy[47]. For this powder and under SPS conditions, the activation energy of densification and grain growth are respectively 536[32] and 575 kJ/mol[34]. From the simple comparison of these activation energies, these very close values do not allow to conclude on a possible advantage of fast heating in minimizing coarsening. In additions, the microstructure of the two specimens reported in figure 5c shows a limited grain growth near ~200 nm. Moreover, the flash SPS test at 1000 K/min has higher grain growth. Because the grain growth limits the densification kinetics, grain growth cannot explain the fast kinetics in our tests.

Starting from above creep parameters (A, n) [32], we test the capacity of theoretical moduli to reproduce the experimental sintering response. We use the moduli of Skorohod [48], Sofronis & McMeeking [49], Green [50]. The latter theoretical moduli consider that spherical porosity shape assumes a dominant surface diffusion mechanism on the porosity skeleton and consequently a low-stress intensification factor. If these theoretical moduli explain the fast sintering kinetics of SPS and flash SPS, this will indicate that there is no impact of microstructure reactivity on the sintering mechanisms.

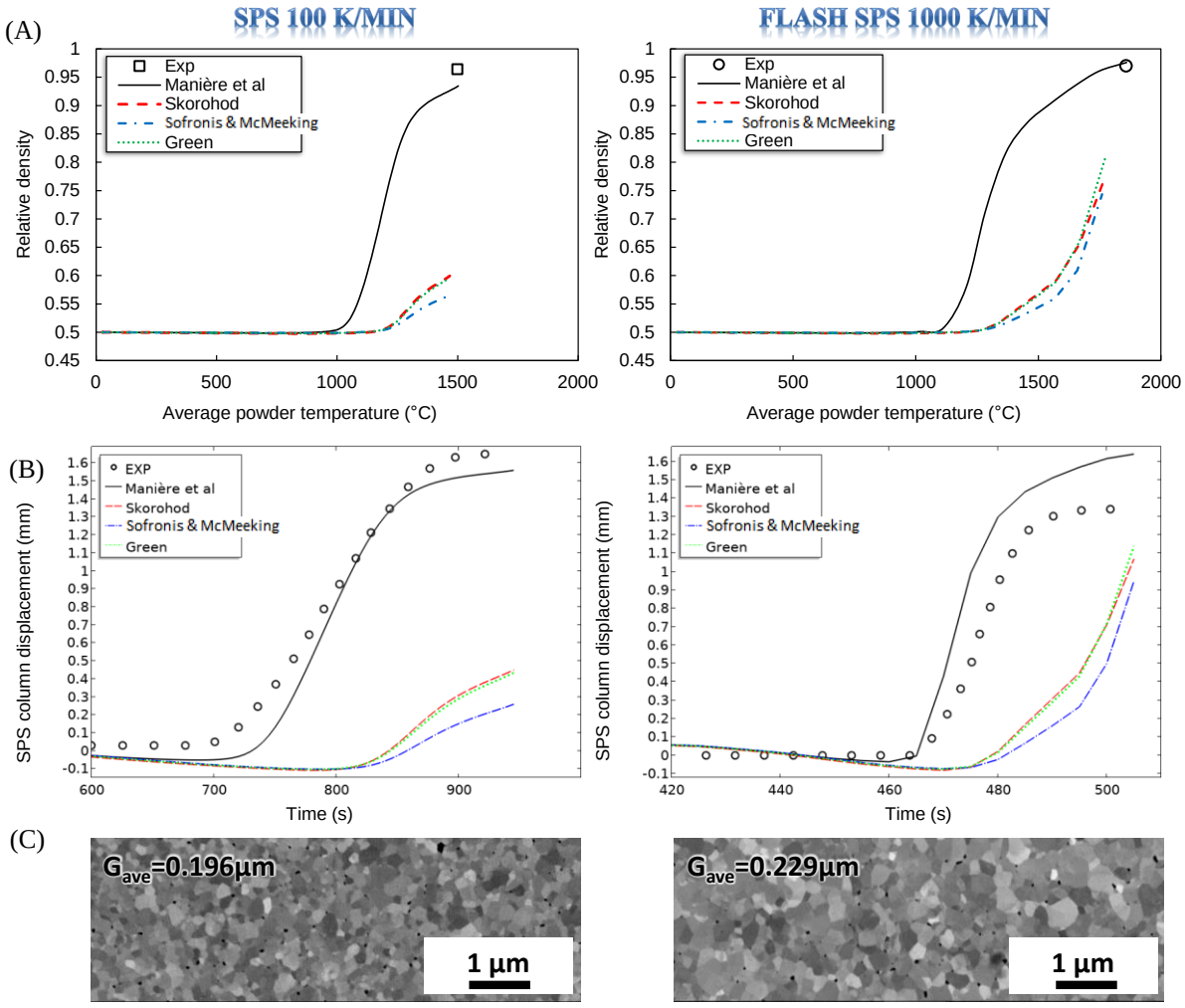

Figure 5 Simulated relative density curves and SPS column displacement for different shear and bulk moduli obtained experimentally (Manière et al) [32] *and by spherical pore theoretical approximation (Skorohod* [48]*, Sofronis & McMeeking* [49]*, Green* [50]*), with (A) the relative density curves, (B) the displacement curves and (C) the final microstructures.*

The simulated relative density and shrinkage curves are reported in figure 5a, 5b, we clearly see the theoretical moduli fail in explaining both the SPS and flash SPS sintering kinetics. The theoretical moduli (based on a low reactive porosity skeleton) give a strongly delayed sintering response compared to the sintering experimental moduli. The errors with final relative density are reported in table 1. This shows that the high values of calculated specimen effective sintering temperature (by FEM) combined with spherical pore moduli do not explain the fast sintering kinetics. Only the experimental moduli (black line in figure 5) allow reproducing the experimental sintering response. The experimental shear and bulk moduli are significantly lower than the theoretical one and result in a higher stress intensification factor

that allows explaining the sintering data. Interestingly, both sintering at 100 K/min and at 1000 K/min are well explained by the experimental moduli that were determined by isothermal/insulated *in situ* SPS experiments with fast heating (100K/min). This seems to indicate that the microstructure reactivity is preserved enough at 100 K/min to explain both SPS and flash SPS sintering kinetics. There is apparently no need to consider any current effect to explain the flash kinetics as the creep and moduli were identified on electrically insulated sinter-forging *in situ* tests. We do not mean the current effects are inactive but simply that the effect of the porosity reactive skeleton shape is sufficient to reproduce the fast sintering kinetics.

Table 1 Comparison of the error of the relative density curves.

Moduli	Experimental moduli [32]	Skorohod [48] (plasticity based)	Green [50] (plasticity based)	Sofronis & McMeeking [49] (creep based n=2)
Final relative density error (%) for 100 K/min	3.2 %	33.4 %	33.4 %	40.1 %
Final relative density error (%) for 1000 K/min	0.1 %	20 %	17 %	23 %

This result shows that the experimental shear and bulk moduli succeed in explaining the flash SPS sintering kinetics. In below section, mesoscale simulations are employed to try to explain these moduli high sintering reactivity by different porous skeleton geometry hypotheses.

4.3. Mesoscale simulation for obtaining the shear and bulk moduli of different particle contact shapes

The principle of the mesoscale simulation is described in section 3 and in figure 3. The shear and bulk moduli are calculated for different porous skeleton shapes from the reactive particle contact shape to the lowest reactive case of equilibrium spherical porosity (torus shape here because of the 2D-axisymmetric approximation). The surface diffusion advancement is

idealized by a particle contact model with different pore tip curvature radii (at the neck). For instance, the porous geometry at a fixed relative density of 85% is reported on figure 6. We can see that for a pore tip radius of 10 nm the porous geometry is circular and at equilibrium. This is the case where the 3D pore geometry is a torus. This case is similar to the spherical pore case which represents the situation of minimal stress intensification (less reactive microstructure). The dimension e_a was used to adjust the thickness of the particle at the contact and explore different relative densities.

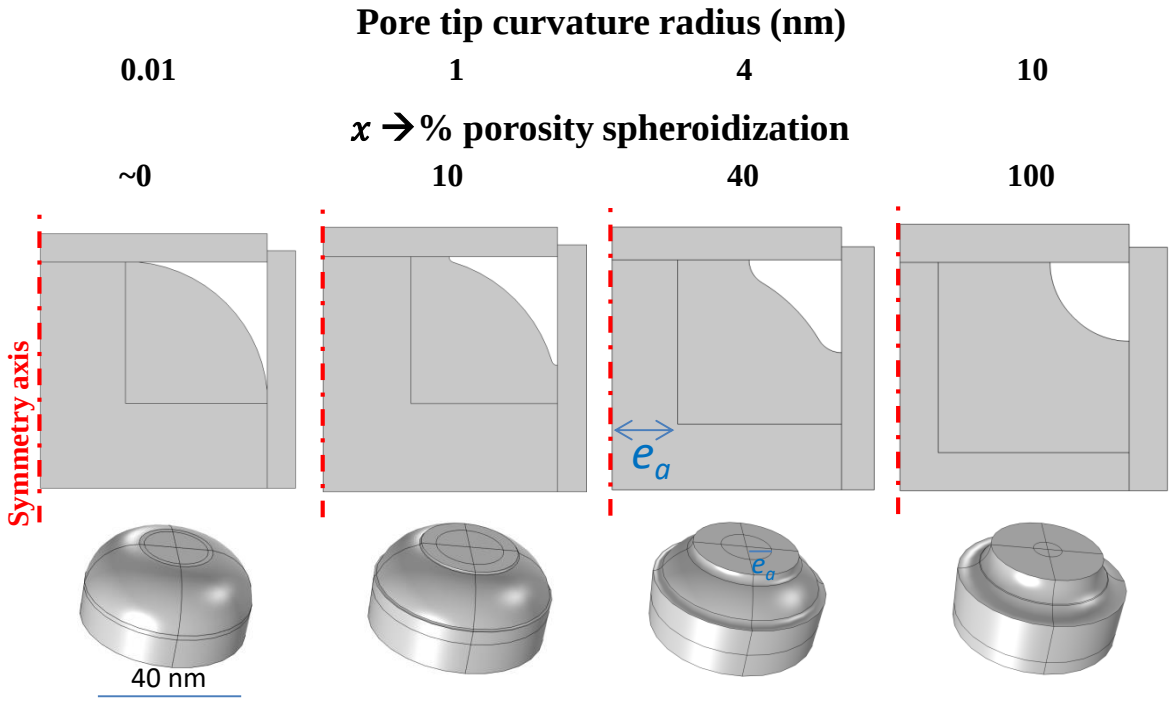

Figure 6 Scheme of the 2D-axisymmetric configuration and corresponding 3D geometry of the mesoscale simulation at a fixed relative density of 85%, the particle size is 40nm.

Using equations (8) that neglect the capillarity pressure (Pl), the simulated shear and bulk moduli reported in figure 7a were obtained. We can see that the moduli curve corresponding to the minimal pore tip curvature radius has the minimum values. Considering the stress intensification factor macroscopic expression (3), this result is expected, the lower the neck radius is, the higher the microstructure reactivity and the stress intensification are. Increasing the pore tip radius gives higher moduli corresponding to less reactive sintering behaviors (lower stress intensification). The evolution of the simulated moduli is logical and reproduces

the expected higher sintering reactivity with lower moduli for the less active surface diffusion geometry.

If the capillarity pressure is considered in the simulation with the identification equation (12), a similar study can be done. The moduli with the P_l term are particularly suited to pressure-less sintering methods like fast firing[51], flash sintering[6] or ultra-fast-high-temperature-sintering[52]. The results are reported in figure 7b. On the contrary to the previous tests, the lowest pore tip radius (0.01) corresponding to the case with almost no surface diffusion was impossible to simulate because the capillarity force at the neck vicinity were too high. The calculated moduli are similarly ordered compared to the case without capillarity pressure. The bulk modulus gives lower values with Pl and the shear modulus curves are slightly higher and with a linear aspect. These simulations (figure 7b) are very sensitive due to the influence of Pl on the estimation of the radial stress used to extract the moduli from the simulation. Consequently, the simulation domain is more restricted than the case where the capillarity pressure is neglected giving relatively close values and a similar behavior. For this reason, in the following discussion, the moduli value neglecting Pl will be preferred to have more stable results.

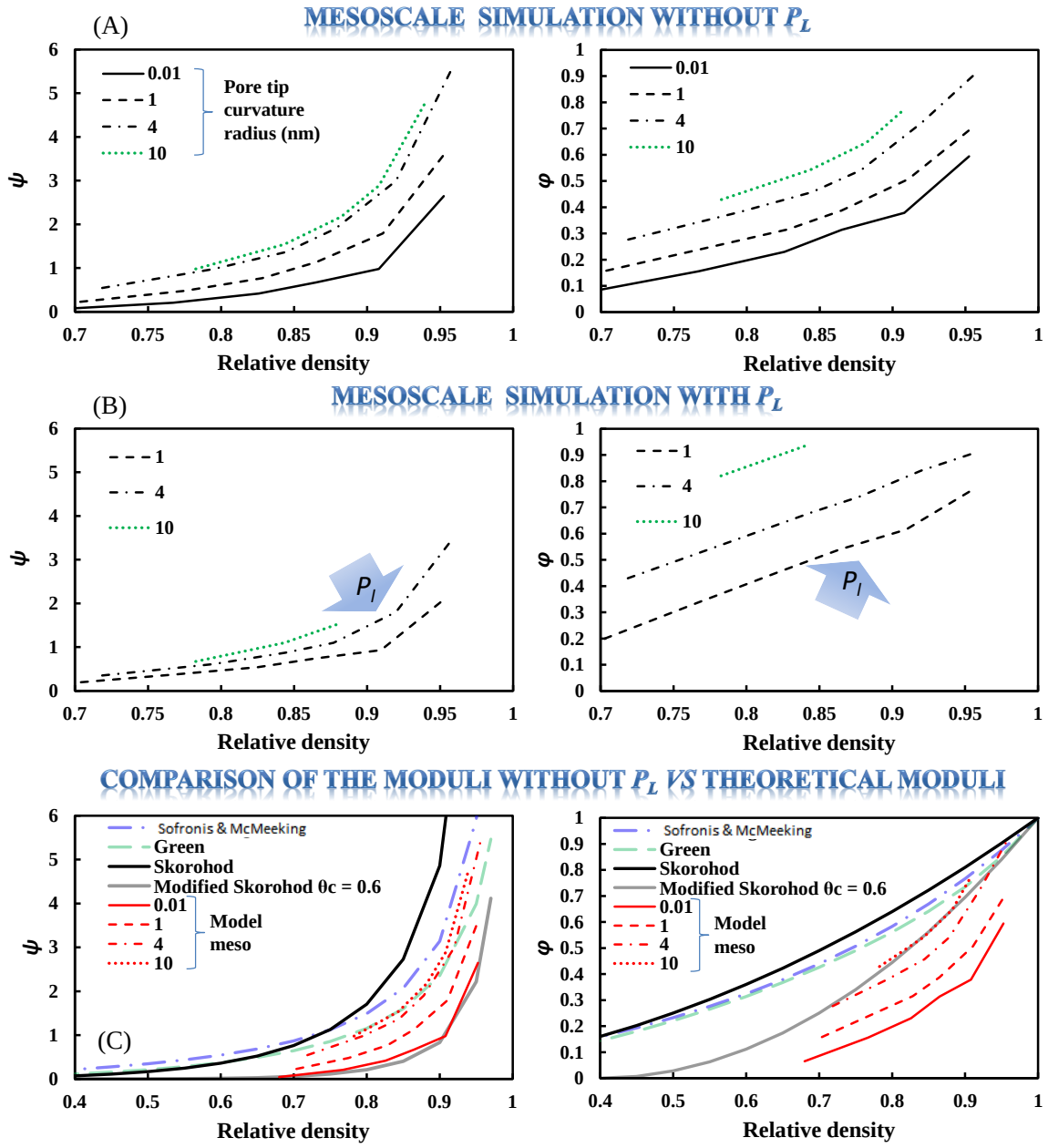

Figure 7 Obtained shear and bulk moduli by mesoscale simulations, without P_l (A), with P_l (B) and comparison of the mesoscale moduli with classic theoretical moduli.

In order to compare the value of the mesoscale moduli, they are compared with the theoretical one in figure 8. Like figure 5, we use the moduli of Skorohod [48], Sofronis & McMeeking [49], Green [50] which assume dominant surface diffusion by a spherical porosity. In figure 8, the theoretical moduli have higher values closer to the simulated moduli with circular porosity. This result is expected as the theoretical moduli simulate the case of low microstructure reactivity and then low stress intensification. In the previous work ref[22], modified Skorohod moduli were used to take into account the initial stage with higher

reactivity with a critical porosity θ_c. The latter corresponds to the initial porosity with a slightly higher value to prevent starting with a singularity. These corrected moduli functions are reported below.

$$\varphi = \left(1 - \frac{\theta}{\theta_c}\right)^2 \quad (16)$$

$$\psi = \frac{2}{3}\frac{(\theta_c - \theta)^3}{\theta} \quad (17)$$

The modified Skorohod moduli with a critical porosity of 0.6 are reported in figure 7c (gray curve). In both cases the modified moduli give lower values corresponding to more reactive sintering behavior. These modified moduli were used in the regression method [23] to correct the free-sintering behavior, giving coherent values of activation energy with other independent methods like the master sintering curves. In figure 7c, the modified bulk modulus corresponds to the case of high reactivity with a very small pore tip radius (0.01). For the modified shear modulus, the low values are observed in the relative density range 0.5-0.6 but for higher values, the decreasing effect of the critical porosity (θ_c) is less effective.

The FEM simulation shows the modified moduli gives a first approximation of the microstructures reactivity. In order to fully match these simulated moduli, the exponent of the moduli in equations (16) and (17) were modified to fit the simulated curves. The fitting equations are reported in figure 8. As shown in figure 6, the pore tip radius evolving from 0.01 to 10nm is associated with a progressive pore skeleton spheroidization noted "*x"*. In figure 8, the evolution of the moduli exponent is related to "*x"*. The moduli exponents decreases in the same function as the porosity spheroidization $\left(\frac{3}{3+x}\right)^{0.24}$. Eventually, this function can be used to help describing the surface diffusion advancement (porosity spheroidization) by comparing the exponent values for this powder. However, this supposes a low impact of the grain rearrangement which is not considered in this study.

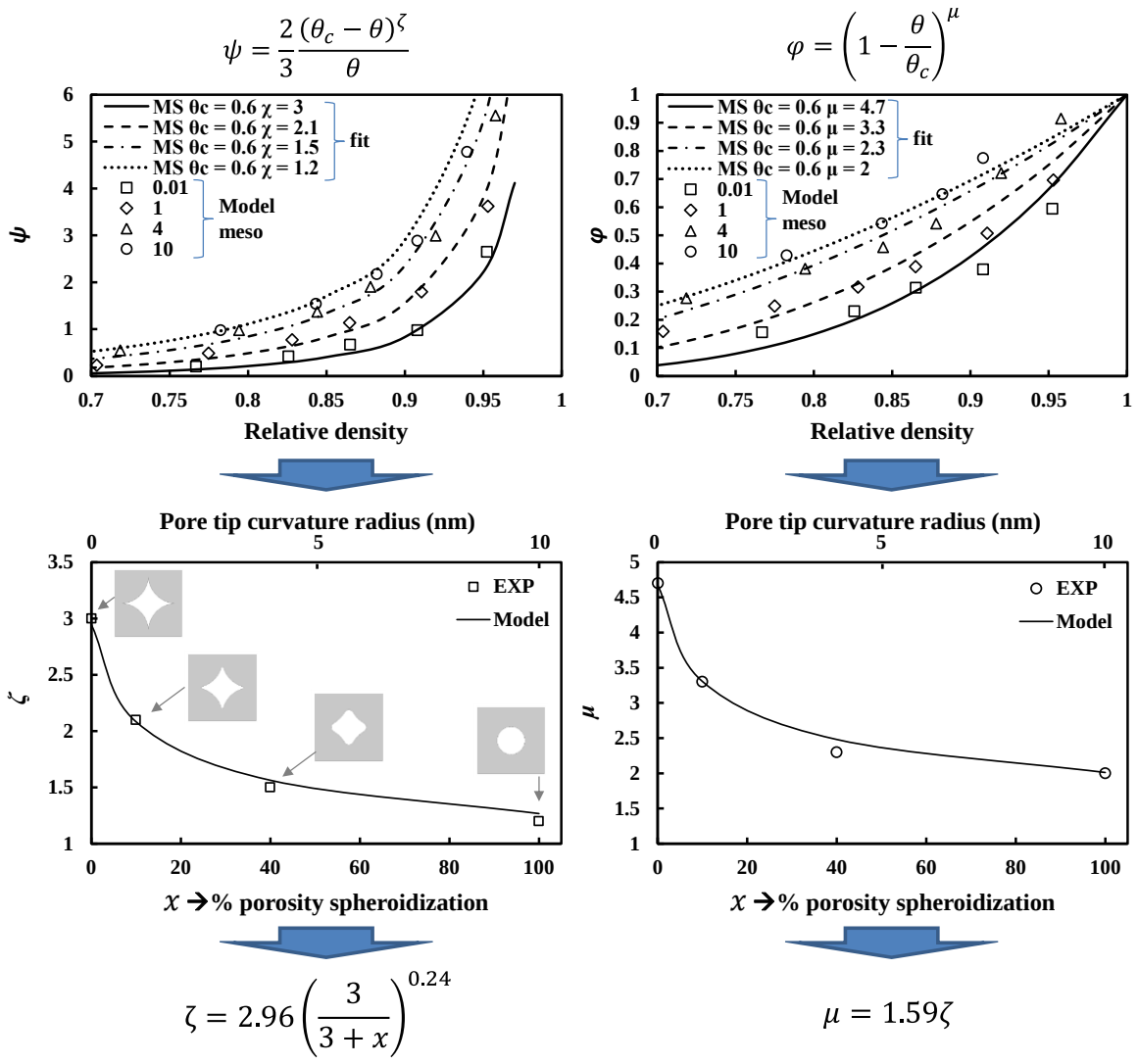

Figure 8 Mathematical fitting of the mesoscale simulated shear and bulk moduli with adjusted exponents to represent the effect of the surface diffusion by the porosity spheroidization x, the scheme below represents the equivalent 2D four grain porosity evolution with different pore tip curvature radii.

4.4. Simulated stress intensification factor vs experimental one.

The shear and bulk moduli have been determined by simulation for a wide range of relative density and porosity spheroidization "*x*". Using the fitted moduli expression in figure 8, and equation (3), the corresponding simulated stress intensification functions are reported in figure 9 as a function of the relative density. As expected, the lower the surface diffusion/spheroidization is the higher the stress intensification factor is. With the experimental moduli equations (13) and (14), the experimental stress intensification factor of zirconia can be compared to the latter mesoscale simulated curves in figure 9. Surprisingly,

the experimental stress intensification points are higher than the simulated curve with the highest pore shape reactivity (x=0). One possible explanation for this difference is the degree of the idealization of the porous skeleton in the simulation. The geometry considered in figure 6 allows considering both the initial stage reactivity and the pore spheroidization. However, real microstructures are not made of regularly ordered particles. Tosoh zirconia has partially agglomerated nanoparticles[53] and like for most powders, the grain arrangement is chaotic. The real porous skeleton should have a higher reactivity by the contribution of the particle rearrangement. The particle rearrangement is very difficult to model at mesoscale because it needs to model about hundred grains in a unit cell which drastically increases the calculation time [54]. A simple approach to model the rearrangement without modeling each particle is to assume the simulated particles is not fully dense but porous. This approach has been used to model the sintering behavior of agglomerated powders [35,55,56]. In figure 9, we have added the simulated curve (bleu curve) corresponding to a reactive pore geometry (x=0) and a particle porosity of 10%. This parameter has a high influence on the stress intensification factor and gives values that can explain the experimental data points.

The high reactivity of the experimental moduli that can reproduce the SPS and flash SPS behaviors seems to be explained by a combination of high porous skeleton reactivity due to delayed surface diffusion and particle rearrangement. Concerning the surface diffusion, Ji *et al* [51] evidence experimentally for zirconia that rapid heating tends to generate finer pore structures compared to conventional heating regardless if an electric field is applied or not. These experiments suggest like for our experimental moduli a reactive microstructure due to delayed surface diffusion.

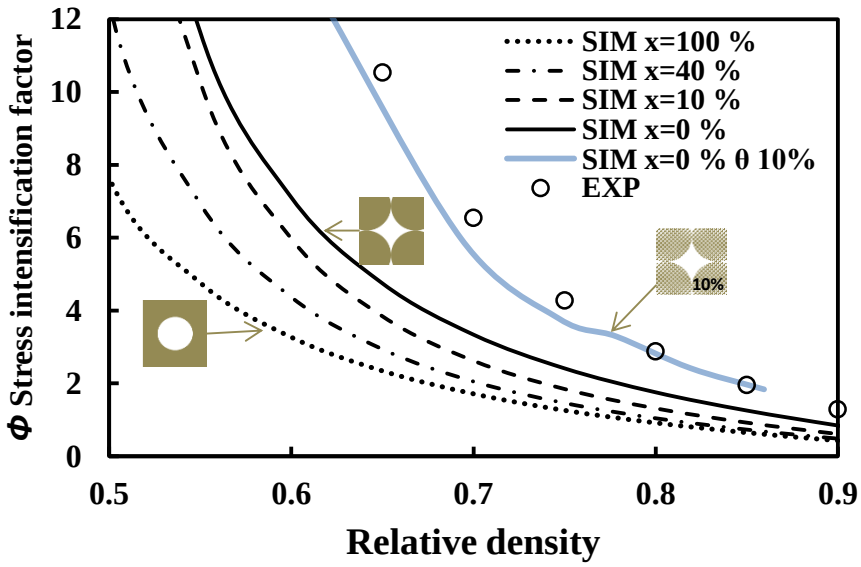

Figure 9 Comparison of the stress intensification factor using the simulated shear and bulk moduli (with x the % of spheroidization) and the experimental moduli, the bleu curve originates from the mesoscale simulated moduli assuming the particles are agglomerates containing 10% of porosity.

4.5. Discussions on experimental evidence of microstructure reactivity

Study the reactivity of nano-size particles flash sintering is difficult as it requires advanced *in situ* TEM equipment able to ultra-fast heat the powder. However, close experiments on ultra-fast pressure-less sintering have been recently disclosed by Phuah *et al*[57] on the same powder. These experiments show fast porosity elimination can result a direct sintering approach where the initial powder reactive sharp skeleton is preserved (see pore called “P3” in figure 10a). It also shows in ultra-rapid ramping profile (5 K/s) that sharp shape of the pores are preserved (see pore called “P8” in figure 10b) if the heating is fast suggesting the surface diffusion has no time to reconfigure the pore shape in a lower surface energy round shape. On the contrary, we made an interrupted test on the same tosoh zirconia at 10 K/min (see figure 10c). In this test, the remaining porosity at 1220°C is high because with previously cold press the sample at a low pressure (20 MPa); this high porosity helps examine the porous skeleton surface that clearly shows a rounded surface shape characteristic of active surface diffusion. These experiments along with others in the literature[52,53,58] show a highly porous skeleton reactivity is preserved if the heating is fast or ultra-fast. They also show the

powder is agglomerated which increase the stress intensification factor from our mesoscale simulations.

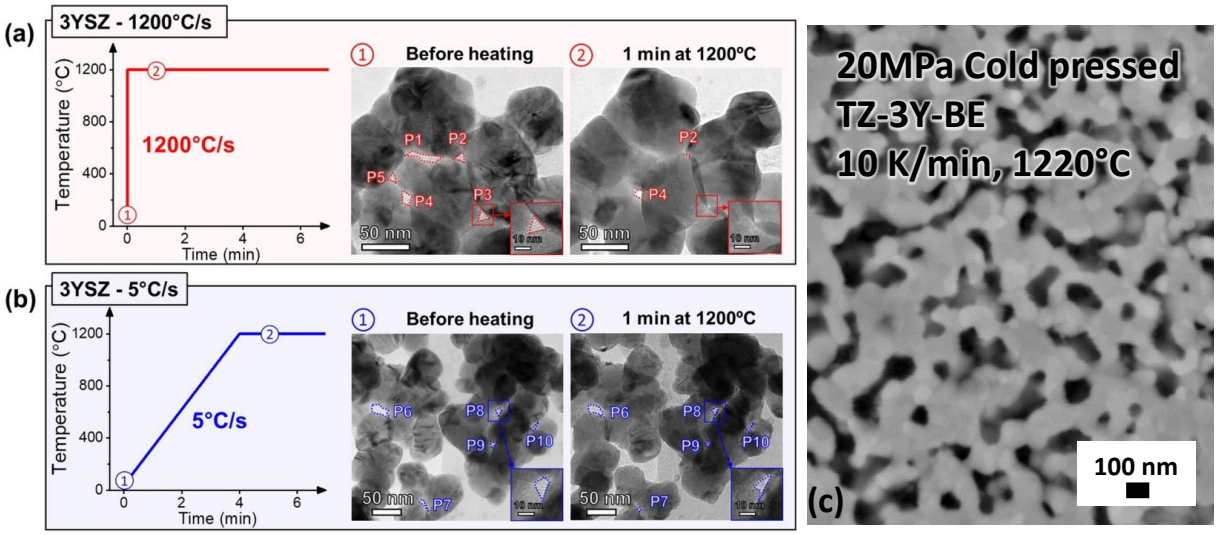

Figure 10 In situ TEM ultra-fast heating experiments in "direct sintering" (a) and "ramping" (b) thermal cycle, reprinted from Phuah et al [57]; These images show the highly preserved sharp porous skeletons compared to a 10 K/min conventionally sintered microstructure which was previously cold pressed in a low pressure to favor coarsening (c), the apparent porous skeleton clearly shows rounded surfaces characteristic of active surface diffusion.

5. Conclusion

In this study, the origin of SPS and flash SPS ultra-rapid sintering kinetics has been studied. High heating rates with sintering time of minutes or seconds may increase the sintering kinetics by delaying (i) the grain growth kinetics, (ii) the pore tip curvature growth (by surface diffusion). Another possible mechanism (iii) is the underestimation of the specimen real temperature by the effect of the thermal contact resistance that raises the temperature differences of few hundreds degrees between the measurement and the specimen, creating an erroneous apparent amplified sintering kinetics. In this study, we tested these three hypotheses by the electro-thermal-mechanical-microstructural simulation of SPS and flash SPS and mesoscale simulation. The first numerical tool is able to estimate the specimen temperatures with the electro-thermal contact resistance effects and the corresponding densification/grain growth response of a zirconia powder. The surface diffusion is not directly explored but by its

impact on the porosity skeleton reactivity and the corresponding shear and bulk moduli. A mesoscale simulation corresponding to different porous skeleton geometries has been used in this aim. From these numerical explorations, the following conclusions can be made:

- First, the Joule heating simulation reveals the temperature of the sample can be 400K and 700K higher in SPS and flash SPS respectively with temperatures exceeding 2000 °C. This thermal response has been coupled to a sintering model that considers both grain growth and the densification kinetic. This shows that using theoretical moduli corresponding to spherical pore skeletons (that assumes dominant surface diffusion), the ultra-rapid sintering response is not explained despite these high modeled temperatures. On the contrary, the sintering curves of SPS and flash SPS are well explained by SPS experimental moduli.

- The experimental moduli of zirconia were determined by SPS isothermal sinter-forging tests with a heating rate of 100K/min. This suggests that contrariwise to conventional sintering, the pressure and the short sintering time of SPS allow identifying experimental moduli with enough reactive microstructures that are less influenced by surface diffusion. Because the sinter-forging tests were conducted in electrically insulated conditions, we can exclude a dominant current effect on these tests.

- Finally, the mesoscale simulations help testing different pore skeleton geometries. This study demonstrates that the high reactivity of the experimental moduli can be explained by a combination of sharp (reactive) pore tip shape (that can result in a very limited surface diffusion) and particles agglomerates rearrangement.

Appendix: Physical properties of the simulated materials

Table A Temperature dependent material properties of electrodes, graphite, and zirconia[34,36].

Materials		Expression
Graphite	*Cp* ($J.kg^{-1}.K^{-1}$)	$34.3+2.72.T-9.6E-4.T^2$
Electrode		$446.5+0.162.T$
Zirconia		$43+2.35.T-4.34E-3.T^2+4.25E-6.T^3-2.09E-9.T^4+4.05E-13.T^5$
Graphite	κ ($W.m^{-1}.K^{-1}$)	$123-6.99E-2.T+1.55E-5.T^2$
Electrode		$9.99+0.0175.T$
Zirconia		$(1.96-2.32E-4.T+6.33E-7.T2-1.91E-10.T3).(1-1.5\theta)$
Graphite	ρ ($kg.m^{-3}$)	$1904-0.0141.T$
Electrode		7900
Zirconia		$(6132-9.23E-2.T-7.26E-5.T^2+4.58E-8.T^3-1.31E-11.T^4).(1-\theta)$
Graphite	σ_{elec} (S/m)	$1/[1.70E-5-1.87E-8.T+1.26E-11.T^2-2.46E-15.T^3]$
Electrode		$1/[(50.2+0.0838.T-1.76E-5.T^2).1E-8]$
Zirconia		$10509.exp(-11920/T).(1-1.5\theta)$ 300-1200K $(0.223.T-267).(1-1.5\theta)$ 1200-1370K $5886.exp(-6894/T).(1-1.5\theta)$ above 1370K
Graphite	α (T^{-1})	$-1.25E-12.T^2+3.68E-9.T+1.33E-6$
Electrode		$4.48E-9.T+1.09E-5$
Zirconia		$-1.31E-12.T^2+3.98E-9.T+5.50E-6$

Acknowledgements

This work was supported by two projects: the French National Research Agency (ANR), project ULTRARAPIDE N°ANR-19-CE08-0033-01 and the project “région normadie” - 00016601-20E02057_RIN RECHERCHE 2020 - Emergent – ULTIMODULUS.

References

[1] M. Biesuz, V.M. Sglavo, Flash sintering of ceramics, J. Eur. Ceram. Soc. 39 (2019) 115–143. doi:10.1016/j.jeurceramsoc.2018.08.048.

[2] R.I. Todd, Flash Sintering of Ceramics: A Short Review, in: Proc. IV Adv. Ceram. Appl. Conf., Atlantis Press, Paris, 2017: pp. 1–12. doi:10.2991/978-94-6239-213-7_1.

[3] M. Yu, S. Grasso, R. Mckinnon, T. Saunders, M.J. Reece, Review of flash sintering: materials, mechanisms and modelling, Adv. Appl. Ceram. 116 (2017) 24–60. doi:10.1080/17436753.2016.1251051.

[4] C.E.J. Dancer, Flash sintering of ceramic materials, Mater. Res. Express. 3 (2016) 102001. doi:10.1088/2053-1591/3/10/102001.

[5] R. Raj, M. Cologna, J.S.C. Francis, Influence of Externally Imposed and Internally Generated Electrical Fields on Grain Growth, Diffusional Creep, Sintering and Related Phenomena in Ceramics, J. Am. Ceram. Soc. 94 (2011) 1941–1965. doi:10.1111/j.1551-2916.2011.04652.x.

[6] M. Cologna, B. Rashkova, R. Raj, Flash Sintering of Nanograin Zirconia in <5 s at 850°C, J. Am. Ceram. Soc. 93 (2010) 3556–3559. doi:10.1111/j.1551-2916.2010.04089.x.

[7] R. Raj, M. Cologna, A.L.G. Prette, V. Sglavo, Methods of flash sintering, Patent US 20130085055 A1, US 20130085055 A1, 2013. https://www.google.com/patents/US20130085055.

[8] G. Lee, E.A. Olevsky, C. Manière, A. Maximenko, O. Izhvanov, C. Back, J. McKittrick, Effect of electric current on densification behavior of conductive ceramic powders consolidated by spark plasma sintering, Acta Mater. 144 (2018) 524–533. doi:10.1016/j.actamat.2017.11.010.

[9] G. Lee, C. Manière, J. McKittrick, E.A. Olevsky, Electric current effects in spark

plasma sintering: From the evidence of physical phenomenon to constitutive equation formulation, Scr. Mater. 170 (2019) 90–94. doi:10.1016/j.scriptamat.2019.05.040.

[10] K.I. Rybakov, E.A. Olevsky, V.E. Semenov, The microwave ponderomotive effect on ceramic sintering, Scr. Mater. 66 (2012) 1049–1052. doi:10.1016/j.scriptamat.2012.02.043.

[11] E.A. Olevsky, A.L. Maximenko, E.G. Grigoryev, Ponderomotive effects during contact formation in microwave sintering, Model. Simul. Mater. Sci. Eng. 21 (2013) 055022. doi:10.1088/0965-0393/21/5/055022.

[12] J.H. Booske, R.F. Cooper, S.A. Freeman, K.I. Rybakov, V.E. Semenov, Microwave ponderomotive forces in solid-state ionic plasmas, Phys. Plasmas. 5 (1998) 1664–1670. doi:10.1063/1.872835.

[13] H. Conrad, Electroplasticity in metals and ceramics, Mater. Sci. Eng. A. 287 (2000) 276–287. doi:10.1016/S0921-5093(00)00786-3.

[14] J. Narayan, A new mechanism for field-assisted processing and flash sintering of materials, Scr. Mater. 69 (2013) 107–111. doi:10.1016/j.scriptamat.2013.02.020.

[15] E. Olevsky, L. Froyen, Constitutive modeling of spark-plasma sintering of conductive materials, Scr. Mater. 55 (2006) 1175–1178. doi:10.1016/j.scriptamat.2006.07.009.

[16] E.A. Olevsky, L. Froyen, Impact of Thermal Diffusion on Densification During SPS, J. Am. Ceram. Soc. 92 (2009) S122–S132. doi:10.1111/j.1551-2916.2008.02705.x.

[17] E.A. Olevsky, S. Kandukuri, L. Froyen, Consolidation enhancement in spark-plasma sintering: Impact of high heating rates, J. Appl. Phys. 102 (2007) 114913. doi:10.1063/1.2822189.

[18] R.I. Todd, E. Zapata-Solvas, R.S. Bonilla, T. Sneddon, P.R. Wilshaw, Electrical characteristics of flash sintering: thermal runaway of Joule heating, J. Eur. Ceram. Soc. 35 (2015) 1865–1877. doi:10.1016/j.jeurceramsoc.2014.12.022.

[19] W. Ji, B. Parker, S. Falco, J.Y. Zhang, Z.Y. Fu, R.I. Todd, Ultra-fast firing: Effect of heating rate on sintering of 3YSZ, with and without an electric field, J. Eur. Ceram. Soc. 37 (2017) 2547–2551. doi:10.1016/j.jeurceramsoc.2017.01.033.

[20] R.K. Bordia, S.-J.L. Kang, E.A. Olevsky, Current understanding and future research directions at the onset of the next century of sintering science and technology, J. Am. Ceram. Soc. 100 (2017) 2314–2352. doi:10.1111/jace.14919.

[21] C. Manière, L. Durand, A. Weibel, C. Estournès, A predictive model to reflect the final

stage of spark plasma sintering of submicronic α-alumina, Ceram. Int. 42 (2016) 9274–9277. doi:10.1016/j.ceramint.2016.02.048.

[22] C. Manière, T. Grippi, S. Marinel, Estimate microstructure development from sintering shrinkage: A kinetic field approach, Mater. Today Commun. 31 (2022) 103269. doi:10.1016/j.mtcomm.2022.103269.

[23] G. Kerbart, C. Harnois, S. Marinel, C. Manière, Modeling the sintering trajectories of MgAl2O4 Spinel, Scr. Mater. 203 (2021) 114048. doi:10.1016/j.scriptamat.2021.114048.

[24] D. Demirskyi, D. Agrawal, A. Ragulya, Comparisons of grain size-density trajectory during microwave and conventional sintering of titanium nitride, J. Alloys Compd. 581 (2013) 498–501. doi:10.1016/j.jallcom.2013.07.159.

[25] M.-Y. Chu, M.N. Rahaman, L.C. Jonghe, R.J. Brook, Effect of Heating Rate on Sintering and Coarsening, J. Am. Ceram. Soc. 74 (1991) 1217–1225. doi:10.1111/j.1151-2916.1991.tb04090.x.

[26] C. Manière, G. Lee, J. McKittrick, S. Chan, E.A. Olevsky, Modeling zirconia sintering trajectory for obtaining translucent submicronic ceramics for dental implant applications, Acta Mater. 188 (2020) 101–107. doi:10.1016/j.actamat.2020.01.061.

[27] M.N. Rahaman, Sintering of Ceramics, CRC Press, 2007.

[28] R.L. Coble, Diffusion Models for Hot Pressing with Surface Energy and Pressure Effects as Driving Forces, J. Appl. Phys. 41 (1970) 4798–4807. doi:10.1063/1.1658543.

[29] E. Arzt, M.F. Ashby, K.E. Easterling, Practical applications of hotisostatic Pressing diagrams: Four case studies, Metall. Trans. A. 14 (1983) 211–221. doi:10.1007/BF02651618.

[30] G.W. Scherer, Sintering inhomogeneous glasses: Application to optical waveguides, J. Non. Cryst. Solids. 34 (1979) 239–256. doi:10.1016/0022-3093(79)90039-5.

[31] S. Shima, M. Oyane, Plasticity theory for porous metals, Int. J. Mech. Sci. 18 (1976) 285–291. doi:10.1016/0020-7403(76)90030-8.

[32] C. Manière, C. Harnois, S. Marinel, Porous stage assessment of pressure assisted sintering modeling parameters: a ceramic identification method insensitive to final stage grain growth disturbance, Acta Mater. 211 (2021) 116899. doi:10.1016/j.actamat.2021.116899.

[33] G. Bernard-Granger, C. Guizard, Spark plasma sintering of a commercially available granulated zirconia powder: I. Sintering path and hypotheses about the mechanism(s) controlling densification, Acta Mater. 55 (2007) 3493–3504. doi:10.1016/j.actamat.2007.01.048.

[34] C. Manière, C. Harnois, G. Riquet, J. Lecourt, C. Bilot, S. Marinel, Flash spark plasma sintering of zirconia nanoparticles: Electro-thermal-mechanical-microstructural simulation and scalability solutions, J. Eur. Ceram. Soc. (2021). doi:10.1016/j.jeurceramsoc.2021.09.021.

[35] E.A. Olevsky, Theory of sintering: from discrete to continuum, Mater. Sci. Eng. R Reports. 23 (1998) 41–100. doi:10.1016/S0927-796X(98)00009-6.

[36] J. Xu, Z. Liu, Z. Xie, S. He, X. Xi, DC electric field-assisted hot pressing of zirconia: methodology, phenomenology, and sintering mechanism, J. Am. Ceram. Soc. (2021) jace.17963. doi:10.1111/jace.17963.

[37] R.L. Coble, Sintering Crystalline Solids. I. Intermediate and Final State Diffusion Models, J. Appl. Phys. 32 (1961) 787–792. doi:10.1063/1.1736107.

[38] O. Guillon, J. Gonzalez-Julian, B. Dargatz, T. Kessel, G. Schierning, J. Räthel, M. Herrmann, Field-Assisted Sintering Technology/Spark Plasma Sintering: Mechanisms, Materials, and Technology Developments, Adv. Eng. Mater. 16 (2014) 830–849. doi:10.1002/adem.201300409.

[39] W. Chen, U. Anselmi-Tamburini, J.E. Garay, J.R. Groza, Z.A. Munir, Fundamental investigations on the spark plasma sintering/synthesis process, Mater. Sci. Eng. A. 394 (2005) 132–138. doi:10.1016/j.msea.2004.11.020.

[40] K. Vanmeensel, A. Laptev, J. Hennicke, J. Vleugels, O. Vanderbiest, Modelling of the temperature distribution during field assisted sintering, Acta Mater. 53 (2005) 4379–4388. doi:10.1016/j.actamat.2005.05.042.

[41] A. Zavaliangos, J. Zhang, M. Krammer, J.R. Groza, Temperature evolution during field activated sintering, Mater. Sci. Eng. A. 379 (2004) 218–228. doi:10.1016/j.msea.2004.01.052.

[42] R. Orrù, R. Licheri, A.M. Locci, A. Cincotti, G. Cao, Consolidation/synthesis of materials by electric current activated/assisted sintering, Mater. Sci. Eng. R Reports. 63 (2009) 127–287. doi:10.1016/j.mser.2008.09.003.

[43] C. Manière, L. Durand, E. Brisson, H. Desplats, P. Carré, P. Rogeon, C. Estournès, Contact resistances in spark plasma sintering: From in-situ and ex-situ determinations

to an extended model for the scale up of the process, J. Eur. Ceram. Soc. 37 (2017) 1593–1605. doi:10.1016/j.jeurceramsoc.2016.12.010.

[44] C. Manière, G. Lee, E.A. Olevsky, All-Materials-Inclusive Flash Spark Plasma Sintering, Sci. Rep. 7 (2017) 15071. doi:10.1038/s41598-017-15365-x.

[45] C. Manière, G. Lee, E.A. Olevsky, Flash sintering of complex shapes, Appl. Mater. Today. 26 (2022) 101293. doi:10.1016/j.apmt.2021.101293.

[46] M.P. Harmer, R.J. Brook, Fast firing - microstructural benefits, Trans. J. Br. Ceram. Soc. 80 (1981) 147–148. http://pascal-francis.inist.fr/vibad/index.php?action=getRecordDetail&idt=PASCAL8130524431.

[47] M.N. Rahaman, Ceramic Processing and Sintering, 2nd Editio, CRC Press, 2017. doi:10.1201/9781315274126.

[48] V.V. Skorohod, Rheological basis of the theory of sintering, Nauk. Dumka, Kiev. (1972).

[49] P. Sofronis, R.M. McMeeking, Creep of Power-Law Material Containing Spherical Voids, J. Appl. Mech. 59 (1992) S88. doi:10.1115/1.2899512.

[50] R.J. Green, A plasticity theory for porous solids, Int. J. Mech. Sci. 14 (1972) 215–224. doi:10.1016/0020-7403(72)90063-X.

[51] W. Ji, J. Zhang, W. Wang, Z. Fu, R.I. Todd, The microstructural origin of rapid densification in 3YSZ during ultra-fast firing with or without an electric field, J. Eur. Ceram. Soc. 40 (2020) 5829–5836. doi:10.1016/j.jeurceramsoc.2020.07.027.

[52] C. Wang, W. Ping, Q. Bai, H. Cui, R. Hensleigh, R. Wang, A.H. Brozena, Z. Xu, J. Dai, Y. Pei, C. Zheng, G. Pastel, J. Gao, X. Wang, H. Wang, J.-C. Zhao, B. Yang, X. (Rayne) Zheng, J. Luo, Y. Mo, B. Dunn, L. Hu, A general method to synthesize and sinter bulk ceramics in seconds, Science (80-.). 368 (2020) 521–526. doi:10.1126/science.aaz7681.

[53] H. Majidi, T.B. Holland, K. van Benthem, Quantitative analysis for in situ sintering of 3% yttria-stablized zirconia in the transmission electron microscope, Ultramicroscopy. 152 (2015) 35–43. doi:10.1016/j.ultramic.2014.12.011.

[54] C.L. Martin, L.C.R. Schneider, L. Olmos, D. Bouvard, Discrete element modeling of metallic powder sintering, Scr. Mater. 55 (2006) 425–428. doi:10.1016/j.scriptamat.2006.05.017.

[55] A.L. Maximenko, E.A. Olevsky, M.B. Shtern, Plastic behavior of agglomerated

powder, Comput. Mater. Sci. 43 (2008) 704–709. doi:10.1016/j.commatsci.2008.01.011.

[56] E.A. Olevsky, R. Rein, Kinetics of sintering for powder systems with bimodal pore-size distribution, High Temp. Press. 27 (1995) 81–90. http://www.oldcitypublishing.com/journals/hthp-electronic-archive-home/hthp-electronic-archive-issue-contents/hthp-volume-27-number-1-1995/.

[57] X.L. Phuah, J. Jian, H. Wang, X. Wang, X. Zhang, H. Wang, Ultra-high heating rate effects on the sintering of ceramic nanoparticles: an in situ TEM study, Mater. Res. Lett. 9 (2021) 373–381. doi:10.1080/21663831.2021.1927878.

[58] D. Wang, X. Wang, C. Xu, Z. Fu, J. Zhang, Densification mechanism of the ultra-fast sintering dense alumina, AIP Adv. 10 (2020) 025223. doi:10.1063/1.5119030.

Figure captions

Figure 1 2D scheme of the porosity spheroidization of a 4-grain model at constant porosity (15%) under the action of surface diffusion; correlation with the stress intensification factor, this shape evolution strategy will be applied in 3D structures of a half particle.

Figure 2 Configuration of the 15mm diameter SPS tests conducted at 100 K/min and 1000 K/min, the location of the two pyrometers and simulation temperature probes are indicated by the red arrow and points.

Figure 3 Geometry of the 3D microstructures approximation in the mesoscale simulation; 2D-axisymmetric simulations at mesoscale, configuration, boundary conditions (A) and simulation capture of the von Mises stress distribution of a pressed particle (B).

Figure 4 FEM Joule heating simulation of the SPS 100 K/min and 1000 K/min flash SPS, simulated thermal field at the end of heating (A), simulated temperature curves at different locations of the pressing device (B), two virtual probes are added to know the specimen temperature at the center and the edge.

Figure 5 Simulated relative density curves and SPS column displacement for different shear and bulk moduli obtained experimentally (Manière et al) [32] and by spherical pore

theoretical approximation (Skorohod [48], Sofronis & McMeeking [49], Green [50]), with (A) the relative density curves, (B) the displacement curves and (C) the final microstructures.

Figure 6 Scheme of the 2D-axisymmetric configuration and corresponding 3D geometry of the mesoscale simulation at a fixed relative density of 85%, the particle size is 40nm.

Figure 7 Obtained shear and bulk moduli by mesoscale simulations, without P_l (A), with P_l (B) and comparison of the mesoscale moduli with classic theoretical moduli.

Figure 8 Mathematical fitting of the mesoscale simulated shear and bulk moduli with adjusted exponents to represent the effect of the surface diffusion by the porosity spheroidization x, the scheme below represents the equivalent 2D four grain porosity evolution with different pore tip curvature radii.

Figure 9 Comparison of the stress intensification factor using the simulated shear and bulk moduli (with x the % of spheroidization) and the experimental moduli, the bleu curve originates from the mesoscale simulated moduli assuming the particles are agglomerates containing 10% of porosity.

Figure 10 In situ TEM ultra-fast heating experiments in "direct sintering" (a) and "ramping" (b) thermal cycle, reprinted from Phuah et al [57]; These images show the highly preserved sharp porous skeletons compared to a 10 K/min conventionally sintered microstructure which was previously cold pressed in a low pressure to favor coarsening (c), the apparent porous skeleton clearly shows rounded surfaces characteristic of active surface diffusion.

Table captions

Table 1 Comparison of the error of the relative density curves.